JOURNAL OF GUIDANCE, CONTROL, AND DYNAMICS
Vol. 27, No. 3, May–June 2004

# Scaling Effects and Dynamic Characteristics of Miniature Rotorcraft

Bernard Mettler,* Chris Dever,† and Eric Feron‡
*Massachusetts Institute of Technology, Cambridge, Massachusetts 02139*

**The dynamic characteristics of miniature rotorcraft, starting from a parameterized linear model developed for the identification of a Yamaha R-50 helicopter (3.04-m rotor diameter), and later applied to a smaller, more agile X-Cell .60 helicopter (1.52-m rotor diameter), are described. From this model, key flying qualities metrics are extracted and related to physical parameters. Based on these metrics, the identified data, and fundamental Froude and Mach scaling hypotheses, the effects of rotorcraft size on flying qualities and performance characteristics are analyzed and scaling trends inferred. These results are used to highlight the mechanical features and flight characteristics that are typical of small-scale rotorcraft, as well as to provide basic design guidelines for this class of vehicles.**

## Nomenclature

| | | |
|---|---|---|
| $A$ | = | rotor disc area |
| $A_b$ | = | blade surface area, longitudinal flapping cross coupling |
| $A_c$ | = | longitudinal flapping stabilizer bar |
| $A_{\text{lat,lon}}$ | = | longitudinal flapping cyclic inputs |
| $a$ | = | main rotor longitudinal flapping angle |
| $\bar{a}_x$ | = | maximum rectilinear acceleration |
| $B_a$ | = | lateral flapping cross coupling |
| $B_d$ | = | lateral flapping stabilizer bar |
| $B_{\text{lat,lon}}$ | = | lateral flapping cyclic inputs |
| $b$ | = | main rotor lateral flapping angle |
| $C_{\text{lon}}$ | = | stabilizer bar cyclic input |
| $c$ | = | stabilizer bar longitudinal flapping angle |
| $c$ | = | rotor chord |
| $c_T$ | = | thrust coefficient |
| $c_\alpha$ | = | lift curve slope |
| $DL$ | = | rotor disc loading |
| $D_{\text{lat}}$ | = | stabilizer bar cyclic input |
| $d$ | = | stabilizer bar lateral flapping angle |
| $e$ | = | rotor hinge offset |
| $\boldsymbol{F}$ | = | linear system stability matrix, Froude number |
| $\boldsymbol{G}$ | = | linear system input matrix |
| $g$ | = | gravitational acceleration |
| $h$ | = | height of main rotor above vehicle c.g. |
| $I_{xx}$ | = | roll axis moment of inertia |
| $I_\beta$ | = | flapping moment of inertia |
| $K_c$ | = | stabilizer bar mechanical mixer gain |
| $K_{r,rfb}$ | = | yaw rate dampings |
| $k_\beta$ | = | rotor effective linear spring constant |
| $L$ | = | characteristic length |
| $L_b$ | = | lateral flapping spring |
| $L_e$ | = | couple due to hinge offset |
| $L_k$ | = | main rotor stiffness moment |
| $(L_p)_e$ | = | effective roll damping |
| $L_T$ | = | thrust vector tilt moment |
| $L_{u,v,w}$ | = | roll rate translational velocities |
| $(L_{\delta_{\text{lat}}})_e$ | = | control sensitivity |
| $\bar{L}$ | = | maximum thrust-to-weight ratio |
| $\boldsymbol{M}$ | = | linear system mass matrix |
| $M_a$ | = | pitch rate flapping |
| $M_{\text{col}}$ | = | pitch rate input |
| $M_{u,v,w}$ | = | pitch rate translational velocities |
| $m$ | = | vehicle mass |
| $N$ | = | length scale factor |
| $N_{\text{col,ped}}$ | = | yaw rate inputs |
| $N_{p,r}$ | = | yaw rate angular velocities |
| $N_{rfb}$ | = | yaw rate feedback |
| $N_{v,w}$ | = | yaw rate translational velocities |
| $P_i$ | = | induced rotor power |
| $p, q, r$ | = | body frame angular velocities |
| $R$ | = | rotor radius |
| $Re$ | = | Reynolds number |
| $r$ | = | rotor inner radius |
| $r_{fb}$ | = | yaw rate feedback state |
| $\boldsymbol{T}$ | = | thrust vector |
| $T$ | = | thrust magnitude, characteristic timescale |
| $\boldsymbol{u}$ | = | linear system input vector |
| $u, v, w$ | = | body frame translational velocities |
| $V$ | = | characteristic velocity |
| $v$ | = | vehicle speed |
| $v_i$ | = | induced inflow velocity |
| $W$ | = | vehicle weight |
| $X_a$ | = | forward velocity flapping |
| $X_u$ | = | forward velocity speed |
| $\boldsymbol{x}$ | = | linear system state vector |
| $Y_b$ | = | lateral velocity flapping |
| $Y_{\text{ped}}$ | = | lateral velocity input |
| $Y_v$ | = | lateral velocity speed |
| $Z_{a,b}$ | = | vertical velocity flappings |
| $Z_{\text{col}}$ | = | vertical velocity input |
| $Z_r$ | = | vertical velocity yaw rate |
| $Z_w$ | = | vertical velocity damping |
| $\beta$ | = | rotor flapping angle |
| $\gamma$ | = | blade Lock number |
| $\delta_{\text{col}}$ | = | collective input |
| $\delta_{\text{lat}}$ | = | lateral cyclic input |
| $\delta_{\text{lon}}$ | = | longitudinal cyclic input |
| $\delta_{\text{ped}}$ | = | pedal input |
| $\Theta_0$ | = | collective setting for steady climb |
| $\theta$ | = | pitch angle |
| $\lambda_i$ | = | induced inflow ratio |
| $\rho$ | = | air density |
| $\rho_{\min}$ | = | minimum turn radius |
| $\sigma$ | = | rotor solidity |

Received 3 February 2003; accepted for publication 7 October 2003. 

*Postdoctoral Associate, Laboratory for Information and Decision Systems, Department of Aeronautics and Astronautics; bmettler@mit.edu. Associate Member AIAA.

†Doctoral Candidate, Charles Stark Draper Laboratory, Department of Mechanical Engineering, 555 Technology Square; cdever@draper.com.

‡Associate Professor, Laboratory for Information and Decision Systems, Department of Aeronautics and Astronautics; feron@mit.edu. Senior Member AIAA.

$\tau$ = flapping time constant
$\tau_p$ = rate response time constant
$\phi$ = roll angle
$\bar{\phi}$ = maximum bank angle
$\Omega$ = rotor angular velocity

*Subscripts*

$f$ = main rotor
$m$ = model vehicle
$p$ = prototype vehicle
$s$ = stabilizer bar

## Introduction

UNMANNED aerial vehicles are the focus of numerous research activities today. Miniature rotorcraft are a particularly interesting subclass of such vehicles. Their compact size and ability to hover, turn on the spot, move in various directions, and cruise similar to fixed-wing aircraft make small-scale rotorcraft well-suited for operations in challenging, dynamic environments. Candidate mission tasks include inspection, surveillance, reconnaissance, delivery, and even object manipulation. Through physical scaling effects, such as increased thrust-to-inertia ratio with decreased vehicle size, small-scale vehicles can be made far more agile than their full-scale counterparts. It is, thus, possible to execute a variety of aggressive and aerobatic maneuvers that are crucial for operation in confined or dynamic surroundings. In addition, compared to traditional full-scale manned vehicles, miniature rotorcraft are fairly inexpensive, easy to transport, and well-suited for coordination with other vehicles and systems.

A fundamental problem in the realization of autonomous miniature rotorcraft operation has been the development of automatic flight-control and guidance systems that effectively exploit the vehicle's natural capabilities. The design of such systems is best accomplished when an appropriate model of the vehicle dynamics describing key response and performance characteristics is available. This is certainly true for model-based techniques such as *LQ* or $H_\infty$. Models are also essential for the analysis of the vehicle's flying qualities and performance, both for the specification of vehicle instrumentation and characterization of operational capabilities.

Early work in automatic control of miniature rotorcraft largely stayed away from the modeling task and used empirically tuned classical feedback controllers.[1–3] This approach was motivated by the difficulties in both the derivation of accurate dynamic models from scratch or the adaptation of existing, detailed full-scale helicopter models.[4] With empirically designed control systems, operation typically has been limited to stationary-type flight, that is, hover and slow-speed trajectory following. These controllers have helped develop other essential systems for automatic flight, such as the onboard computer, navigation systems, path planning systems, and even computer vision systems.[1]

To be practical for control design and analysis purposes, a vehicle model must be simple, yet accurately predict dynamic responses in a broad range of operating conditions. Linear models are typically preferred because there are numerous effective linear control design methodologies available. However, rotorcraft often require multiple linear models scattered across the flight envelope, capturing changes in dynamic behavior during a typical flight. Moreover, unlike fixed-wing aircraft, which are often sufficiently modeled with rigid-body equations of motion,[5] rotary-wing vehicles display significant coupling effects between rotor and fuselage motions. Such effects play a critical role in defining vehicle response in the mid- to high-frequency range[6] and require additional system states to incorporate properly into the model.[7] However, when rotorcraft are modeled with standard first-principles approaches, this quickly results in complex high-order nonlinear equations of motion that carry an excessive level of detail, contain numerous unknown parameters, and are often poorly suited for direct control design. Therefore, to obtain a useful vehicle model, we seek a method that combines basic physical principles, an understanding of vehicle flight characteristics, and insight gathered from experimental data.

The coupling of physical and system identification-based modeling has proven an effective method for the generation of simple and accurate models for full-scale manned rotorcraft. These models are typically used for flight-control design and flying qualities (FQ) analysis.[8] To date, efforts in the application of such techniques to small-scale vehicles have obtained a comparatively small share of the results demonstrated on full-scale rotorcraft. Most studies have focused on a subset of rotorcraft degrees of freedom, often resulting in single-input/single-output linear transfer functions, for example, longitudinal dynamics[9] or angular dynamics.[10,11] Occasionally, models restricted to rigid-body dynamics were used that, although useful for quasi-steady applications, naturally have substantially limited bandwidth[11] and cannot capture high-order physical effects. Note also that all of these earlier efforts concentrated only on hover flight conditions, and, in some cases, experiments were performed on a mechanical rig instead of an actual flying vehicle.[10,11]

In an effort to study small-scale rotorcraft dynamics and generate a useful multivariable model, established system identification methods, including the software package CIFER,[12] were applied first to an instrumented Yamaha R-50 miniature helicopter (667 N, 3.04-m main rotor diameter)[13] and later to a smaller instrumented X-Cell .60 helicopter (75.6 N, 1.52-m rotor diameter)[14] (Fig. 1). The CIFER process has two major parts: first, multivariable input–output data from flight experiments are processed into frequency responses; second, a user-provided parametric linear model is fitted to the estimated responses by the use of nonlinear optimization.

Small-scale rotorcraft typically feature the same main rotor–tail rotor configuration as full-scale helicopters. As such, the development of the parameterized model was based loosely on those used for full-scale rotorcraft identification,[8,15,16] whereas the full-scale flight-test techniques[17] were closely adapted to the remotely piloted miniature vehicle. To help human pilots compensate for control sensitivity increases brought on by scaling effects, small-scale vehicles are typically equipped with a stabilizer bar, for example, a Bell–Hiller system,[10,18] and an active yaw rate damping system. Because of their strong influence on vehicle dynamic behavior, it was important to account for these stability augmentations in the model explicitly. In addition, scaling effects and numerous miniature helicopter design details also influence the way mechanical and aerodynamic effects play into the overall vehicle dynamics. To determine which effects are most relevant for small-scale rotorcraft, the modeling-identification process was approached iteratively, starting with a baseline model structure[19] that was later augmented with additional states.[13,20] This model refinement process was guided by intermediate identification results, with particular insight provided by numerical sensitivity and statistical metrics computed within the CIFER package.

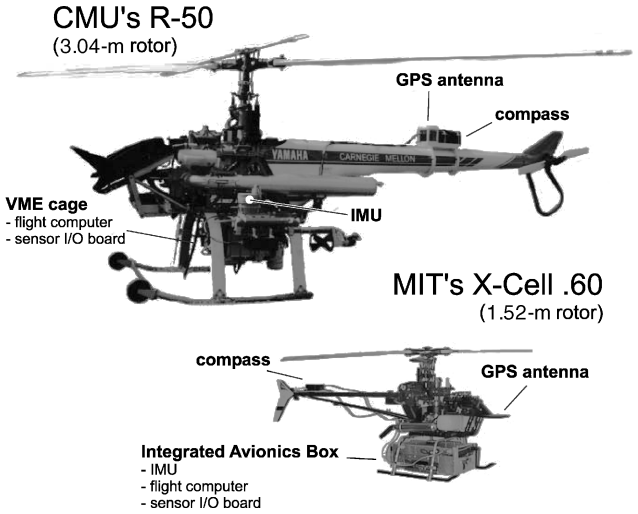


**Fig. 1 CMU's Yamaha R-50 and MIT's X-Cell helicopters with custom instrumentation.**

The resulting full-order model has 13 states ($u, v, p, q, \phi, \theta, a, b, w, r, r_{fb}, c,$ and $d$) and contains a reasonable number of parameters (around 30). The model's multi-input/multi-output structure means that it can be used with multivariable control design methods and that its identification takes full advantage of all available measurements from the coupled vehicle motion. This depth enhances the amount of information available for the identification and produces physically meaningful parameter estimates. The model's accuracy was validated by the use of time domain verification methods, in which flight-test data were compared to model-predicted responses. Although the presented model is linear, it has been shown valid for large control deflections (up to 100% magnitude) and large state deviations (up to maximum physical angular rates). Its form has also been shown to be applicable to the forward cruise flight condition without modification. Many of the model parameters have direct physical meaning, so that identified values can be compared to laboratory measurements of vehicle characteristics, for example, mass, inertia, rotor head stiffness, physical dimensions, etc., which provides a validation of the model's physical significance. Explicit accommodation for the rotorcraft stability augmentations helps to better separate their effects from the underlying bare-airframe characteristics and to obviate their interaction with external flight-control systems.[21,22] Subsequent application of the model structure to a smaller X-Cell .60 helicopter demonstrated its usefulness as a general model for miniature rotorcraft.

When the dynamics of miniature rotorcraft are captured at two important flight regimes (hover and forward cruise), the linear model made possible development of more broadly descriptive nonlinear models[14,23] that were used in realistic full-envelope simulation. Also, use of both the linear and nonlinear models for control analysis allowed a method for easy implementation of multivariable control design techniques.[22] The flight performance attained with such a control system far exceeded what was achieved with the earlier decoupled control systems and enabled even advanced aerobatic maneuvers.[24,25]

Presently, the model is useful for the study of flying qualities for miniature vehicles, a viewpoint not taken in earlier small-scale rotorcraft research. As demonstrated in this paper, it is descriptive of vehicles over widely ranging scales, without a need for significant revision. Thus, by the examination of rotorcraft from a scaling perspective, it is possible to discern the role of physical size in governing bare-airframe dynamic characteristics, FQs, controllability, and frequency response shapes. These considerations are critical when a flight-control system is constructed for a new vehicle design because they will determine the required level of modeling detail, the frequency range that should be explored during identification, and the requisite control system complexity and instrumentation to achieve a performance target.

This paper takes a detailed look at the influence of physical scale on performance characteristics. The main contribution is a quantification of scale as a parameter in vehicle dynamics and a broader description of rotorcraft "dynamic classes," in which a relatively small set of physical parameters may be used to classify the agility (or maneuverability) of a given rotorcraft. Interestingly, the derived scaling laws, which have at their core a small set of physical quantities, extend beyond the realm of small-scale rotorcraft and may even be used to describe full-scale vehicles such as the Bell UH-1H and Robinson R22. The scaling laws quantify the intuitive notion that even though the Yamaha R-50 and X-Cell .60 are both considered miniature helicopters by the general aerospace community, their dynamic characteristics are quite different and, thus, belong to significantly different classes of vehicle. This scale-based viewpoint of dynamics helps the engineer determine what rotorcraft classes are most suitable for various applications and directly aids in the vehicle design task.

The paper opens with a description of several special airframe features of miniature rotorcraft. The parameterized linear model follows with a summary of identification results and physical validation. A detailed application of FQs to small-scale vehicles comes next. Finally, scaling hypotheses based on Froude and Mach considerations are presented with several small- and large-scale helicopters given as examples.

## Airframe Characteristics

Small-scale helicopters, such as the Yamaha R-50 and those used by hobby remote control (RC) pilots, are essentially reduced-size versions of traditional full-scale rotorcraft. A main rotor is employed to generate lift, propulsive forces, and attitude moments, and an antitorquing tail rotor controls the vehicle's yaw moment. The mechanical realization of these devices is virtually identical to their full-scale counterparts. The tail rotor speed is mechanically driven at a fixed multiple of the main rotor rate, which is itself regulated to a near-constant value by an electronic governor. In addition to these similarities with full-scale helicopters, small-scale rotorcraft can possess the following extra features of note.

### Rotor Head Design

Most small-scale rotorcraft use two-bladed rotors; like many larger manned helicopters, the details of the rotor head design can vary significantly from vehicle to vehicle. For example, the Yamaha R-50 uses a trihinge head (one teetering hinge and two independent blade flapping hinges) with elastomeric restraints (Fig. 2). In contrast, the X-Cell .60 uses an unhinged teetering head with harder elastomeric restraints, resulting in a significantly stiffer rotor head. The latter design is prevalent in miniature RC helicopters because rotor head stiffness generally translates into agile maneuvering capabilities, whereas the R-50's more compliant head suits its less aggressive flight requirements. However, because these rotors produce small damping moments in comparison to larger helicopters, both designs feature stabilizer bars for ease of pilot handling.

### Stabilizer Bars

Small-scale rotorcraft are often equipped with a mechanical Bell–Hiller stabilizer bar that effectively applies lagged rate feedback to the two cyclic control channels. This system may be regarded as a secondary rotor attached to the shaft either above or below the main rotor by an unrestrained teetering hinge. The blades consist of two aerodynamic paddles attached at the extremities of an essentially rigid rod. Like the main rotor, the stabilizer bar receives cyclic pitch and roll inputs from the swashplate (but no collective input, unlike the main rotor).

The stabilizer bar itself does not produce significant forces on the helicopter body. Instead, a mechanical mixer connects the stabilizer

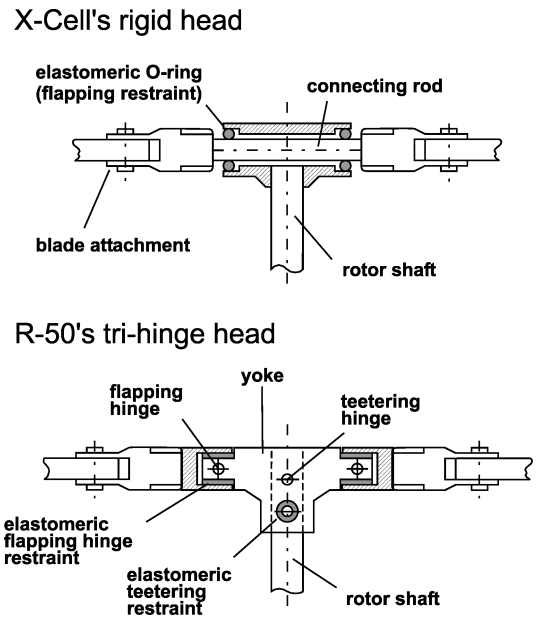


**Fig. 2 X-Cell .60 and Yamaha R-50 rotor head designs showing the main blade attachments.**

bar to the main rotor blade pitch links, augmenting the blade pitch with a component proportional to the stabilizer bar flapping angle (Fig. 3). During steady roll, for example, the main rotor disk will lag behind the rotor shaft by an angle $(\tau_f + B_d\tau_s)p$, instead of merely $\tau_f p$ without the stabilizer bar, producing a greater damping moment on the helicopter and, thus, making the vehicle easier to control manually. Detailed treatment of the stabilizer bar is available in Refs. 10, 18, and 26. A first-order stabilizer bar model, developed for system identification, is also given in the next section.

#### Yaw Rate Damping

An additional stabilizing feature present in many smaller helicopters is yaw rate damping. As with the roll and pitch motions, yaw moments generated by the tail rotor easily produce large angular accelerations, even for small control inputs; thus, they make the rotorcraft hard to control manually. A proportional yaw rate feedback signal is, therefore, added to the pilot's pedal input to provide additional damping.

## System Identification

The linear rotorcraft model presented here accurately predicts responses to pilot inputs and is well-suited for control system design and FQ studies. This section gives its state-space form and describes the identification process used to determine its parameter values.

#### Parameterized State-Space Model

The parameterized model used for identification was developed based on a hybrid rigid-body first-order tip-path-plane rotor formulation employed for full-scale rotorcraft.[15] Model augmentations account for the stabilizer bar and yaw rate feedback system. Through iterative model revision coupled with system identification, we adjusted the structure to capture the dynamics of small-scale helicopters with the smallest set of physically meaningful parameters. Mettler et al.[13] describe the model's detailed development.

Figure 4 shows the model in the state-space form

$$\boldsymbol{M}\dot{\boldsymbol{x}} = \boldsymbol{F}\boldsymbol{x} + \boldsymbol{G}\boldsymbol{u} \tag{1}$$

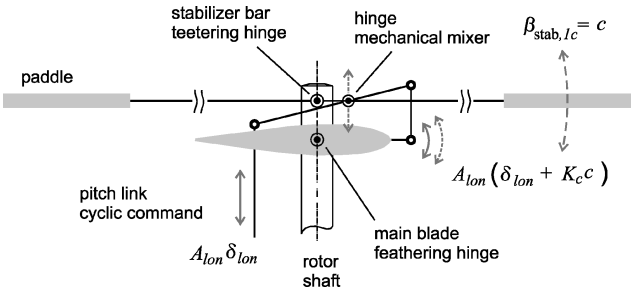


**Fig. 3 Stabilizer bar mechanization.**

with state vector $\boldsymbol{x}$ and input vector $\boldsymbol{u}$. The system matrix $\boldsymbol{F}$ contains the stability derivatives; the input matrix $\boldsymbol{G}$ contains the input derivatives; and the matrix $\boldsymbol{M}$ contains the rotor time constants featured in the blade flapping equations. The actuator dynamics, not shown in the state-space model for clarity, were accounted for during the identification.[13]

Note that in addition to standard relations for vehicle rigid-body dynamics (states $u$, $v$, $w$, $p$, $q$, $r$, $\phi$, and $\theta$), the model includes simplified relations for the rotor, stabilizer, and active yaw damping system. The dynamics of the coupled rotor–stabilizer system are modeled by a pair of first-order tip-path-plane equations of motion for both the rotor and stabilizer bar lateral and longitudinal flapping.

For example, the longitudinal main rotor flapping $a$ is governed by the standard tip-path-plane equation of motion, augmented to include the stabilizer bar contribution:

$$\tau_f\dot{a} = -\tau_f q - a + A_c c + A_{\text{lon}}\delta_{\text{lon}} \tag{2}$$

The stabilizer bar longitudinal flapping is modeled similarly, that is,

$$\tau_s\dot{c} = -\tau_s q - c + C_{\text{lon}}\delta_{\text{lon}} \tag{3}$$

The stabilizer bar is coupled to the main rotor through the derivative $A_c$, which represents the gain $K_c$ of the mechanical mixer (cf. Fig. 3):

$$A_c = A_{\text{lon}}K_c \tag{4}$$

The main rotor is coupled to the fuselage pitch dynamics through the rotor flapping derivative $M_a$:

$$\dot{q} = M_a a \tag{5}$$

A similar set of equations is used for the lateral rotor and stabilizer bar flapping (states $b$ and $d$, respectively) and roll dynamics. For simplicity, the equations shown here account only for first-order effects. Cross-coupling terms and secondary effects are visible in the state-space equation shown in Fig. 4.

FQ studies are typically based on a lower-order model than that given in Fig. 4. In such situations, the identified model can be effectively reduced and still account for the vehicle stability augmentations, as will be shown in the subsequent FQ section.

Given a sensible model structure, the identification problem becomes one of choosing parameter values that reflect the particular vehicle under study. Of course, rotorcraft combine many mechanical and aerodynamic effects, and a complete direct determination of all of the model parameters requires a wide range of experiments and tools (dynamic balance, gyroscopes, wind tunnel, etc.). Also note that the parameterized model is, by necessity, a simplification of a complex nonlinear dynamic system and cannot explicitly account for every physical effect. In fact, during identification, some state-space quantities such as speed sensitivities and input gains may capture effects unmodeled in the structure of Fig. 4. In (fortunate) instances when a parameter can be inferred from both system identification and direct measurement, information from the two sources

$$\begin{bmatrix} \dot{u} \\ \dot{v} \\ \dot{p} \\ \dot{q} \\ \dot{\phi} \\ \dot{\theta} \\ \tau_f\dot{a} \\ \tau_f\dot{b} \\ \dot{w} \\ \dot{r} \\ \dot{r}_{fb} \\ \tau_s\dot{c} \\ \tau_s\dot{d} \end{bmatrix} = \begin{bmatrix} X_u & 0 & 0 & 0 & 0 & -g & X_a & 0 & 0 & 0 & 0 & 0 & 0 \\ 0 & Y_v & 0 & 0 & g & 0 & 0 & Y_b & 0 & 0 & 0 & 0 & 0 \\ L_u & L_v & 0 & 0 & 0 & 0 & 0 & L_b & L_w & 0 & 0 & 0 & 0 \\ M_u & M_v & 0 & 0 & 0 & 0 & M_a & 0 & M_w & 0 & 0 & 0 & 0 \\ 0 & 0 & 1 & 0 & 0 & 0 & 0 & 0 & 0 & 0 & 0 & 0 & 0 \\ 0 & 0 & 0 & 1 & 0 & 0 & 0 & 0 & 0 & 0 & 0 & 0 & 0 \\ 0 & 0 & 0 & -\tau_f & 0 & 0 & -1 & A_b & 0 & 0 & 0 & A_c & 0 \\ 0 & 0 & -\tau_f & 0 & 0 & 0 & B_a & -1 & 0 & 0 & 0 & 0 & B_d \\ 0 & 0 & 0 & 0 & 0 & 0 & Z_a & Z_b & Z_w & Z_r & 0 & 0 & 0 \\ 0 & N_v & N_p & 0 & 0 & 0 & 0 & 0 & N_w & N_r & N_{rfb} & 0 & 0 \\ 0 & 0 & 0 & 0 & 0 & 0 & 0 & 0 & 0 & K_r & K_{rfb} & 0 & 0 \\ 0 & 0 & 0 & -\tau_s & 0 & 0 & 0 & 0 & 0 & 0 & 0 & -1 & 0 \\ 0 & 0 & -\tau_s & 0 & 0 & 0 & 0 & 0 & 0 & 0 & 0 & 0 & -1 \end{bmatrix} \begin{bmatrix} u \\ v \\ p \\ q \\ \phi \\ \theta \\ a \\ b \\ w \\ r \\ r_{fb} \\ c \\ d \end{bmatrix} + \begin{bmatrix} 0 & 0 & 0 & 0 \\ 0 & 0 & Y_{ped} & 0 \\ 0 & 0 & 0 & 0 \\ 0 & 0 & 0 & M_{col} \\ 0 & 0 & 0 & 0 \\ 0 & 0 & 0 & 0 \\ A_{lat} & A_{lon} & 0 & 0 \\ B_{lat} & B_{lon} & 0 & 0 \\ 0 & 0 & 0 & Z_{col} \\ 0 & 0 & N_{ped} & N_{col} \\ 0 & 0 & 0 & 0 \\ 0 & C_{lon} & 0 & 0 \\ D_{lat} & 0 & 0 & 0 \end{bmatrix} \begin{bmatrix} \delta_{lat} \\ \delta_{lon} \\ \delta_{ped} \\ \delta_{col} \end{bmatrix}$$

**Fig. 4 Parameterized linear state-space model for Eq. (1).**

may be combined or simply used to validate the state-space model's physical significance.

### Frequency Domain System Identification

The system identification of both the Yamaha R-50 and X-Cell .60 employed the CIFER identification tool developed jointly by the U.S. Army and NASA[15] and successfully used to analyze full-scale rotorcraft such as the BO 105 and tilt-rotor XV-15. CIFER first transforms multivariable input–output flight data into frequency response estimates by the use of a chirp-z transform, multisignal correlation conditioning, and composite windowing. These responses form a nonparametric frequency domain model of the vehicle. Figures 5 and 6 show the cyclic input-to-roll and pitch body rate responses for the R-50 and X-Cell. These curves resemble second-order systems; the peaks arise from the lightly damped coupled rotor–fuselage mode. The sharp phase roll-off beyond the natural frequency is due to the presence of a pure time delay.

Although only roll and pitch response curves are shown here, additional responses are required to account for other system inputs. Choice of which input–output pairs to estimate is a user design judgement (as described in Ref. 13). During the flight experiment, each of the four input channels were individually selected and repeatedly excited with an increasing-frequency chirp signal, whereas the three remaining off channels were used to maintain a reasonably steady operating point. All flight experiments were flown by

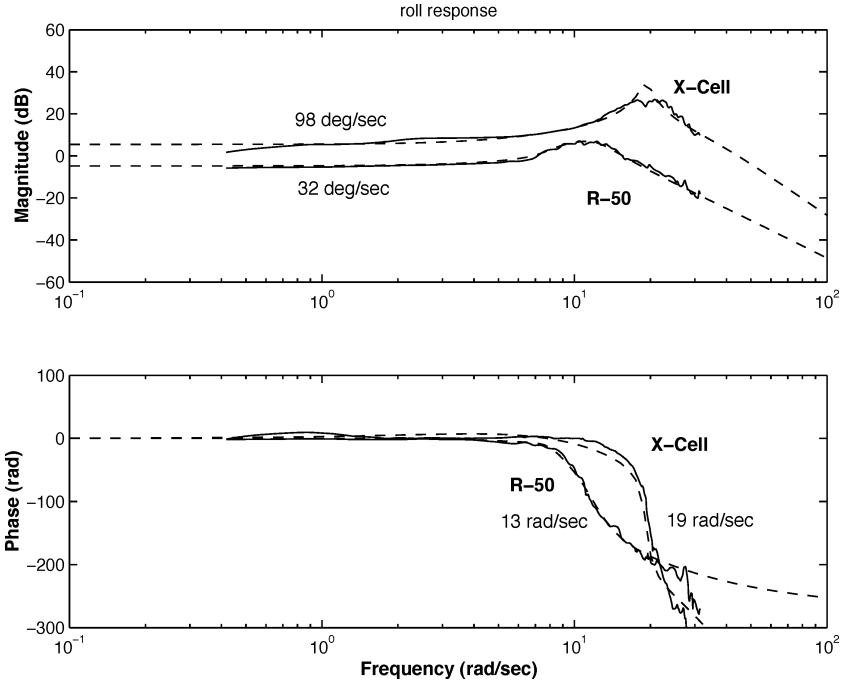


**Fig. 5 Lateral cyclic-to-roll rate frequency responses for the R-50 and X-Cell in hover: ——, response estimated from flight data and - - - -, identified model response; angular rate responses (rate sensitivity) are shown attained at 1 rad/s for full-deflection cyclic input and 135-deg phase bandwidths (control inputs normalized relative to maximum deflection).**

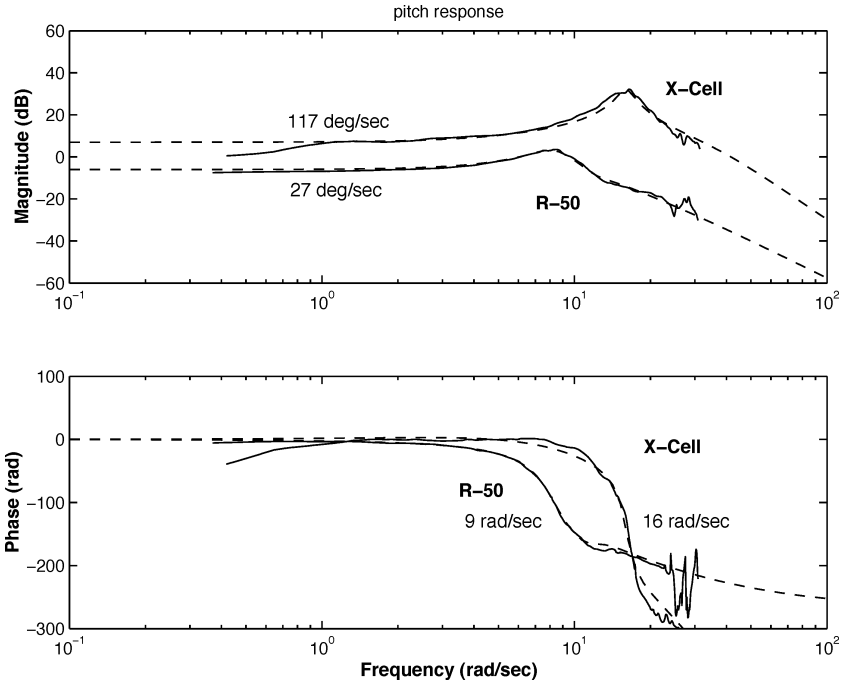


**Fig. 6 Longitudinal cyclic-to-pitch rate frequency responses for the R-50 and X-Cell in hover. ——, response estimated from flight data and - - - -, identified model response; angular rate responses (rate sensitivity) are shown attained at 1 rad/s for full-deflection cyclic input and 135-deg phase bandwidths.**

**Table 1 Identified Yamaha R-50 and X-Cell .60 parameters in hover**

| Angular dynamics parameters | X-Cell | R-50 | Ratio |
|---|---|---|---|
| $\tau_f$ | 0.052 | 0.046 (0.048)[a] | 1.1 |
| $\tau_s$ | 0.22 | 0.34 (0.38) | 0.65 |
| $L_b$ | 320 | 166 (140) | 1.9 |
| $M_a$ | 204 | 82.6 (84.2) | 2.5 |
| $A_b$ | 0[b] | −0.189 (N.A.) | —— |
| $B_a$ | 0[b] | 0.368 (N.A.) | —— |
| $A_c$ | 1.15 | 0.644 (0.68) | 1.8 |
| $B_d$ | 1.15 | 0.71 (0.95) | 1.6 |
| $A_{\text{lat}}$ | 0[b] | 0.015 (N.A.) | —— |
| $A_{\text{lon}}$ | 0.53 | 0.05 (N.A.) | 11 |
| $B_{\text{lat}}$ | 0.42 | 0.07 (N.A.) | 6.0 |
| $B_{\text{lon}}$ | 0[b] | −0.007 (N.A.) | —— |
| $C_{\text{lon}}$ | 0.11 | 0.13 (N.A.) | 0.85 |
| $D_{\text{lat}}$ | 0.11 | 0.135 (N.A.) | 0.81 |

[a]Values in parentheses are analytic predictions for the R-50.
[b]Derivatives were set to zero.

an expert RC helicopter pilot; no closed-loop control authority was present other than yaw rate feedback.

The second phase of the CIFER identification procedure is a numerical search for the state-space model parameters that best match the nonparametric frequency response estimates. Iterative algorithms minimize a weighted frequency domain objective function using a nonlinear secant search. The resulting parameter estimates for the R-50 and X-Cell are given in Table 1. Note from Table 1 that in certain cases, we may compare a parameter's estimate to analytical predictions. The next section gives examples of how to do so. Figures 5 and 6 show the match between the collected roll and pitch frequency responses and those predicted by the identified state-space model. The close agreement of a single model structure for both vehicles validates its physical significance.

The final stage of the identification is time domain model validation, which is normally performed by comparison of predicted and measured time responses to steplike pilot inputs. Results of these validations showed that the model predicted the response to pilot inputs with a high level of accuracy.[13,14] We next look at the validity of the model from a first principles perspective.

## Experimental Validation of Key Derivatives

A number of physical parameters can be determined from direct measurements and/or simple experiments. The following are examples of meaningful physical quantities and the techniques used to measure them. Values obtained through this process will be used in analytic expressions for key model derivatives:

1) Fuselage inertias indicate that rotorcraft principal moments of inertia can be measured from a torsional pendulum test. The oscillation period depends explicitly on the vehicle inertia.[27] Different body axes may be analyzed by orientation of the vehicle appropriately on the pendulum platform.

2) Rotor effective spring indicates that stiffness can be measured from a force-deflection test.

3) Stabilizer bar gearing indicates that the ratio of main rotor blade cyclic input contributions from the swashplate and stabilizer bar can be determined from the geometry of the mechanical Bell–Hiller mixer or through deflection measurements.

4) Main blade and stabilizer bar inertias indicate that flapping inertias can usually be determined from a simple pendulum test.

Values for these and other quantities for the R-50 are given in Table 1 (for the X-Cell, no data from the specific airframe configuration flown during the flight-test experiments were available). The next section illustrates the usefulness of these quantities in estimating some of the state-space derivatives (Fig. 4 and Table 1).

Analytic expressions for some parameters and derivatives are obtainable from classical rotorcraft theory.[28] Table 1 shows the comparison between the identified values and those predicted by analytical expressions.

**Table 2 Physical parameters of the Yamaha R-50 and X-Cell .60 (thrust $T$ corresponds to the hover value)**

| Parameters | X-Cell | R-50 | Ratio |
|---|---|---|---|
| $T$, N | 77 | 680 | 0.11 |
| $I_{xx}$, kg · m$^2$ | 0.18 | 5.98 | 0.03 |
| $I_{yy}$, kg · m$^2$ | 0.35 | 9.99 | 0.035 |
| $h$, m | 0.24 | 0.57 | 0.42 |
| $k_\beta$, N · m/rad | 112 | 471 | 0.24 |
| $I_\beta$, kg · m$^2$ | 0.035 | 1.18 | 0.03 |
| $\gamma_f$ | 2 | 3.8 | 0.53 |
| $\gamma_s$ | 0.58 | 0.51 | 1.1 |
| $k_\beta/Th$ | 6.1 | 1.2 | 5.3 |

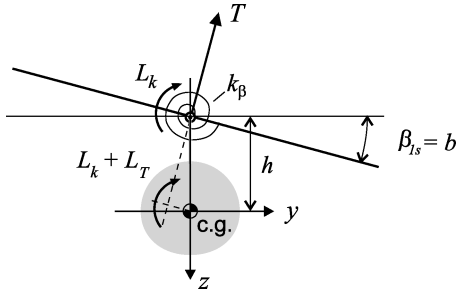


**Fig. 7 Primary flapping moments on fuselage around roll axis.**

*Flapping Derivatives*

Rotor flapping produces a moment on the helicopter fuselage due to three effects. The first contribution $L_k$ comes from the rotor head mechanical stiffness (both teetering and flapping hinge rotor heads may be restrained by elastomeric springs). This stiffness is idealized as a rotor head-centered torsional spring with effective linear spring constant $k_\beta$. The second contribution $L_T$ results from the tilting of the thrust vector $\boldsymbol{T}$ at a height $h$ above the helicopter center of gravity. Finally, for hinged rotors, the centrifugal forces acting on the two blades can produce a couple $L_e$ on the aircraft body.[29] Figure 7 shows the first two of these moments for the roll axis. Identical effects apply to the pitch axis.

If we neglect the offset moment $L_e$, the lateral flapping spring derivative $L_b$ will contain only the thrust vector tilt and rotor stiffness contributions, normalized by the roll moment of inertia:

$$L_b = (1/I_{xx})(k_\beta + Th) \tag{6}$$

A similar expression can be derived for the longitudinal spring derivative $M_a$.

The agreement between the R-50's identified and theoretical values for $L_b$ and $M_a$ derivatives is very good. Note that for a given helicopter, the ratio $k_\beta/Th$ gives a measure of the rotor head's ability to produce a control moment beyond the nominal thrust vector-induced moment. As shown in Table 2, this ratio for the X-Cell is more than fivefold that of the Yamaha R-50, consistent with the relative agility of the two vehicles. Note also that the moment resulting from head stiffness is not dependent on rotor thrust and plays an important role in aerobatic-type flight.

*Rotor and Stabilizer Bar Time Constants*

The first-order time constant for an idealized teetering rotor is given by[28]

$$\tau = 16/\gamma\Omega \tag{7}$$

The Lock number $\gamma$ gives the ratio of aerodynamic to inertial forces acting on the blade and is expressed in terms of physical quantities as

$$\gamma = \left[\rho c c_\alpha (R^4 - r^4)\right] \Big/ I_\beta \tag{8}$$

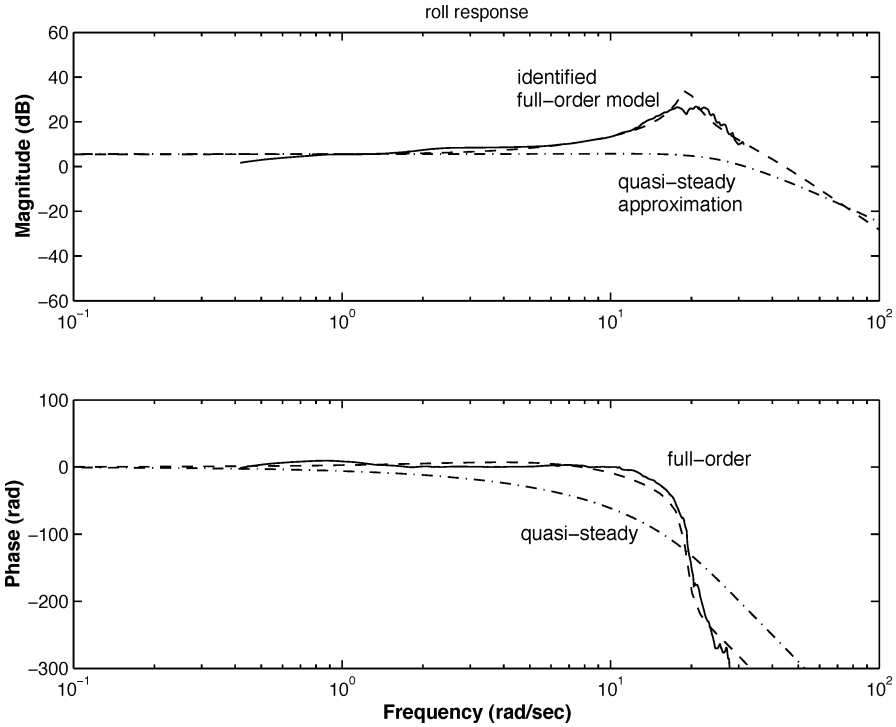


**Fig. 8 Identified X-Cell: ——, lateral cyclic-to-roll rate frequency response in hover; - - - -, predicted full-order model; and · · · ·, predicted quasi-steady model.**

There is usually a significant difference between the main rotor and stabilizer bar Lock numbers, that is, $\gamma_f > \gamma_s$, and, thus, we expect $\tau_s > \tau_f$, as verified in Table 1.

The R-50's identified and predicted values show very good agreement. Given that the combined lagged rate feedback of the main rotor and stabilizer bar tend to slow vehicle attitude motion, $\tau_s/\tau_f$ ratios of 4.2 and 7.4 for the X-Cell and Yamaha, respectively, demonstrate the stabilizer bar's significant contribution to the vehicle's angular damping and, thus, reduced peak angular rate.

*Stabilizer Bar Gearing*

The stabilizer bar gearing $K_c$ for lateral and $K_d$ for longitudinal determines the change in main blade pitch angle produced by stabilizer bar flapping [recall Fig. 3 and Eq. (4)]. To determine the value of $K_c$ ($K_d$ should be equal), we measured the main blade pitch angle for several stabilizer bar flapping angles and obtained the gearing value by taking suitable ratios. The derivatives $A_c$ and $B_d$ can be obtained by application of Eq. (4). Again, good agreement is obtained for the R-50.

## Angular Flying Qualities and Performance Metrics

Once its physical parameters are estimated, the state-space model reveals basic FQs and performance metrics for the rotorcraft under study. The FQs are relevant because they describe mathematically the responsiveness and agility of a vehicle. Because most of the metrics follow from a six-degree-of-freedom rigid-body model, it is necessary to reduce the higher-order state-space to this form by the use of steady-state approximations of the main rotor and stabilizer bar dynamics.

### Quasi-Steady Attitude Dynamics Approximation

To condense the state-space model to rigid-body form, the dynamic rotor and stabilizer bar states are replaced by their steady-state values and then substituted into the angular rate equations of motion. This approach is valid when the first-order flapping time constant is fast compared to the vehicle rigid-body dynamics.

Given the roll channel as an example, the lateral rotor and stabilizer bar flapping derivatives are set to zero, that is, $\dot{b} = \dot{d} = 0$, which gives the steady-state expressions

$$b = -\tau_f p + B_d d + B_{\text{lat}}\delta_{\text{lat}} \tag{9}$$

$$d = -\tau_s p + D_{\text{lat}}\delta_{\text{lat}} \tag{10}$$

Note that all off-axes terms are discarded. Elimination of the variable $d$ gives

$$b = -(\tau_f + B_d\tau_s)p + (B_{\text{lat}} + B_d D_{\text{lat}})\delta_{\text{lat}} \tag{11}$$

The steady-state flapping expressions can now be inserted into the rigid-body equations of motion to obtain the expression for the quasi-steady roll dynamics:

$$\dot{p} = -L_b(\tau_f + B_d\tau_s)p + L_b(B_{\text{lat}} + B_d D_{\text{lat}})\delta_{\text{lat}} \tag{12}$$

The longitudinal channel can be treated similarly. The standard rotorcraft flying qualities metrics are now applicable.[8,29]

Figures 8 and 9 show the frequency responses obtained from the X-Cell quasi-steady model compared to the full-order identified dynamics. Notice that the quasi-steady model does not capture the coupled rotor–fuselage mode and leads to mismatches in both the magnitude and phase in the mid- to high-frequency region. However, it does predict the quasi-steady (low-frequency) rate response accurately. For a helicopter with a high coupled rotor–fuselage natural frequency, the quasi-steady model will be accurate to first-order up to higher frequencies.

### Angular Dynamics Flying Qualities

Key roll flying qualities parameters include (longitudinal metrics obtained similarly) the following:

1) Effective roll damping represents the damping moment produced by the rotor. Note that the stabilizer bar increases the damping moment by an amount $L_b B_d \tau_s$, thus, improving pilot handling:

$$(L_p)_e = -L_b(\tau_f + B_d\tau_s) \tag{13}$$

2) Control sensitivity represents the aerodynamic control moment. Note that the stabilizer bar increases the control sensitivity by

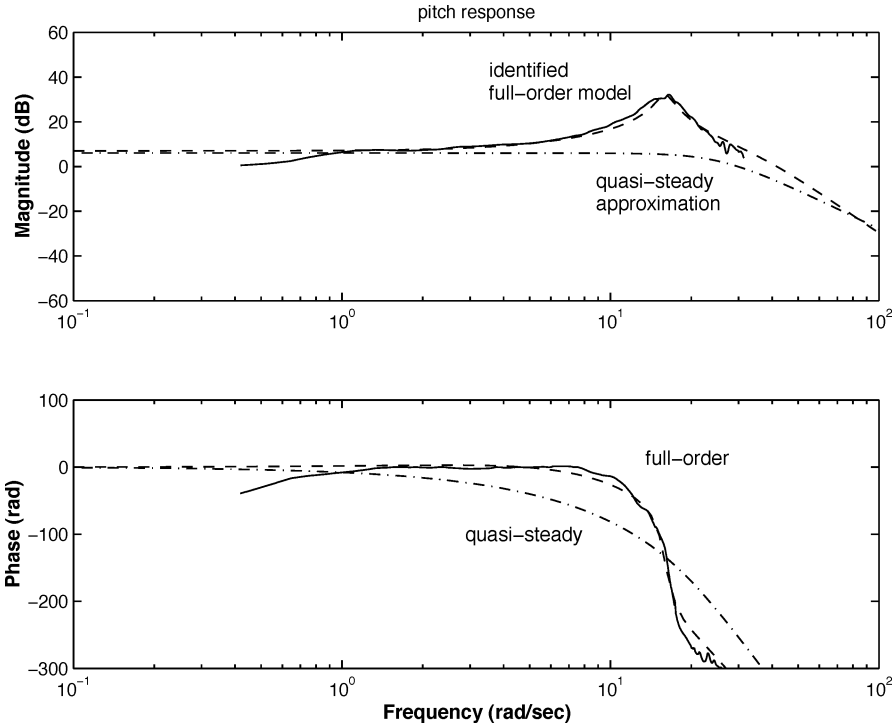


**Fig. 9 Identified X-Cell: ————, longitudinal cyclic-to-pitch rate frequency response in hover; - - - -, predicted full-order model; and - · · · -, predicted quasi-steady model.**

**Table 3 Lateral flying qualities parameters with and without stabilizer bar and scaling effects based on Froude and Mach considerations**

| | Stabilizer bar | | Scaling | |
|---|---|---|---|---|
| Parameter | With | Without | Froude | Mach |
| Effective roll damping, $\frac{1}{\text{s}}$ | $-L_b(\tau_f + B_d\tau_s)$ | $-L_b\tau_f$ | $\sqrt{N}$ | $N$ |
| Control sensitivity, $\frac{\text{rad/s}^2}{\%^{\text{a}}}$ | $L_b(B_{\text{lat}} + B_d D_{\text{lat}})$ | $L_b B_{\text{lat}}$ | $N$ | $N^2$ |
| Rate sensitivity, $\frac{\text{rad/s}}{\%^{\text{a}}}$ | $\frac{B_{\text{lat}} + B_d D_{\text{lat}}}{\tau_f + B_d\tau_s}$ | $\frac{B_{\text{lat}}}{\tau_f}$ | $\sqrt{N}$ | $N$ |
| Rate response time constant, s | $[L_b(\tau_f + B_d\tau_s)]^{-1}$ | $(L_b\tau_f)^{-1}$ | $\frac{1}{\sqrt{N}}$ | $\frac{1}{N}$ |

[a]Percentage refers to fraction of full-stick deflection.

an amount $L_b B_d D_{\text{lat}}$, boosting pilot authority:

$$(L_{\delta_{\text{lat}}})_e = L_b(B_{\text{lat}} + B_d D_{\text{lat}}) \tag{14}$$

3) Rate sensitivity represents the steady-state roll rate the aircraft will attain for a given input. Defined as the ratio of control sensitivity to effective damping. The stabilizer bar makes the vehicle more manageable by reducing the maximum obtainable angular rate:

$$\left.\frac{p(s)}{\delta_{\text{lat}}(s)}\right|_{s=0} = \frac{B_{\text{lat}} + B_d D_{\text{lat}}}{\tau_f + B_d\tau_s} \tag{15}$$

4) The rate response time constant gives the timescale for angular reactions to input steps:

$$\tau_p = [L_b(\tau_f + B_d\tau_s)]^{-1} \tag{16}$$

Table 3 summarizes these FQ parameters both in the presence and absence of the stabilizer bar. (Scaling terms are discussed in the next section.) Figures 5 and 6 show the frequency responses estimated from the flight-test data evaluated for rate sensitivity and phase bandwidth. The X-Cell has a significantly larger rate sensitivity, as well as a faster coupled rotor–fuselage mode.

Key quantities for the angular dynamics include the following:

1) $L_b$, which governs roll moment due to lateral rotor flapping. A stiffer rotor head will have a higher value and, hence, greater control sensitivity but also greater damping.

2) The main rotor and stabilizer bar time constants $\tau_f$ and $\tau_s$. By design, the stabilizer bar dominates the overall rotor response.

3) $B_{\text{lat}}$ and $D_{\text{lat}}$, indicate that lateral stick to lateral cyclic blade pitch gearing is dictated by the main rotor's mechanical design. Relative magnitude varies widely from vehicle to vehicle (cf. Table 1).

4) $B_d$ is the main rotor cyclic blade pitch augmentation due to stabilizer bar flapping. Determined by mechanical design, the mixing coefficient weights the main rotor and stabilizer bar time constants.

## Effect of Size on Rotorcraft Dynamics

Small-scale helicopters operate in the same environment as their full-scale counterparts, but can exhibit substantially different dynamic behavior. For example, the X-Cell .60 is capable of agile aerobatic maneuvers well beyond the reach of virtually all larger vehicles. This section qualitatively describes such variations in rotorcraft dynamics from a scaling viewpoint. The investigation considers the application of two hypotheses: Froude and Mach scaling. Each scaling hypothesis imposes a particular set of relations among a vehicle's physical parameters, most notably rotor size and speed. Given a set of vehicle data, these scaling laws readily quantify to what degree two vehicles may be expected to behave dynamically similar, that is, to have response and FQs that seem to be alike, even if the vehicles are of different sizes. Alternatively, the laws can detect if two rotorcraft, such as the R-50 and X-Cell, will behave differently and possess substantially different flight capabilities. Taken a step further, the Froude and Mach scaling viewpoints describe the scale and rotor speed-dependent variations of the following: thrust-to-weight ratio and the translational flight envelope, rotor performance, angular responsiveness to control inputs (and, thus, agility), and combined rotational and translational maneuverability.

Scaling approaches have been used in other rotorcraft analysis problems as well. For example, in Ref. 30 the authors use Froude scaling to extrapolate full-scale dynamic and stability characteristics

from reduced-scale models. In Ref. 31, both Froude and Mach laws are applied to the aeroelastic scaling problem for rotary-wing vehicles.

When comparing two vehicles, we will state that a model exists at a physical scale $N$ relative to some given prototype, meaning that $R_m = R_p/N$. Thus, a scale factor $N$ denotes a helicopter $1/N$th the size of its prototype.

#### Froude Models

Froude-scaled models have the quality of being dynamically similar to some prototype system. Here, a model and prototype are said to be dynamically similar if the relative magnitudes of their governing forces are unchanged by scale. Froude models are typically used to study systems at reduced size and perhaps reduced cost. Recall that in this setting, the principal rotorcraft forces are inertial, gravitational, and aerodynamic in nature.

To find scaling rules useful in the enforcement of dynamic similarity between two rotorcraft, consider the Froude number

$$\boldsymbol{F} = V^2/Lg \tag{17}$$

If $V$ is taken as the main rotor tip speed and $L$ is taken as the main rotor radius, then $\boldsymbol{F}$ reflects the ratio of blade lift, which is used to produce translational accelerations and rotational moments, to vehicle weight. Given this choice of characteristic $V$ and $L$, equal Froude numbers between two vehicles implies the following relationship between main rotor speeds:

$$\Omega_m = \sqrt{N}\Omega_p \tag{18}$$

When the argument is extended to vehicle timescales $T_m$ and $T_p$, it must hold that

$$T_m = \left(1/\sqrt{N}\right)T_p \tag{19}$$

A summary of physical dimensions related by the Froude scaling law is given in Table 4.

#### Mach Models

Clearly, all rotorcraft are not dynamically similar, and we need additional insights to relate helicopter behavior across scale. A useful consideration is main rotor tip speed, which places an upper limit on a rotorcraft's forward velocity. This restriction exists because high translational velocities can lead to excessive airspeed on the advancing rotor blade (and, therefore, flow compressibility) and insufficient speed on the retreating rotor blade (leading to blade stall). As such, if two vehicles at different scales have similar translational speed envelopes, they are expected to have similar rotor tip speeds. However, given the difference in scale, it is possible that they will exhibit a significant dissimilarity in overall dynamic behavior.

**Table 4 Froude and Mach scaling rules**

| Dimension | Froude | Mach |
|---|---|---|
| Length | $L_m = L_p/N$ | $L_m = L_p/N$ |
| Time constant | $T_m = T_p/\sqrt{N}$ | $T_m = T_p/N$ |
| Speed | $V_m = V_p/\sqrt{N}$ | $V_m = V_p$ |
| Weight | $W_m = W_p/N^3$ | $W_m = W_p/N^3$ |
| Moment of inertia | $I_m = I_p/N^5$ | $I_m = I_p/N^5$ |
| Frequency | $\omega_m = \omega_p\sqrt{N}$ | $\omega_m = \omega_p N$ |

Consider two helicopters, with relative scale $N$ but equal tip speed, that is,

$$\Omega_p R_p = \Omega_m R_m \tag{20}$$

Because their rotor radii follow $R_m = R_p/N$, we must have

$$\Omega_m = N\Omega_p \tag{21}$$

and also the following relation between time constants:

$$T_m = (1/N)T_p \tag{22}$$

Comparing the rotor speed constraint of Eq. (18) to that of Eq. (20), we note that vehicles with similar tip speeds (said to exhibit "Mach similarity") cannot be dynamically similar. In fact, as the next section will show, Mach scaling represents a significant departure from dynamic similarity and helps explain the extreme agility of some small-scale rotorcraft.

Table 4 gives further Mach scaling rules for other physical quantities, again under the assumption that the model and prototype have equal vehicle densities and operate in equal density air.

To demonstrate the applicability of the aforementioned Froude and Mach scaling hypotheses, consider physical data from the Yamaha R-50 and X-Cell .60, as well as two full-scale manned helicopters: the Bell UH-1H and Robinson R22, all of which have two main rotor blades. Table 5 lists physical data for these rotorcraft, including weight, rotor radius, and nominal main rotor speed. The R-50 and X-Cell are given with both nominal (empty) and instrumented weights. The calculated scale ratios use the R-50 as a fixed reference, so that larger vehicles have $N < 1$ and the smaller X-Cell has $N > 1$.

The computed vehicle Froude numbers indicate fairly similar blade lift to gravitational force ratios for the UH-1H, R22, and R-50, whereas the X-Cell Froude number reveals a vehicle whose lift forces are proportionately much larger than its weight.

Noticing that the X-Cell is indeed dynamically dissimilar from the other sample vehicles, we instead examine the rotor tip Mach numbers listed in Table 5. Whereas the UH-1H, R22, and R-50 have differing Mach numbers, the R-50 and X-Cell share similar tip speeds, indicating that the Mach scaling rules of Table 4 will help relate these vehicles' dynamics. Next, the scaling relationships allow certain predictions of helicopter operation, ranging from rotor performance to angular flying qualities.

#### Application of the Scaling Rules

In the following, we apply the scaling rules to study vehicle size-dependent variations in basic rotor parameters. Then, we use the results to make predictions of rotor performance and angular flying qualities parameters. The insight gained will make possible basic predictions about the impact of scale on the maneuvering characteristics of helicopters.

##### *Main Rotor Parameters*

The rotor thrust coefficient is defined by

$$c_T = T/\rho A(\Omega R)^2 \tag{23}$$

Using this formula, and the scaling laws of Table 4, we can determine how the hover thrust coefficient will change for both

**Table 5 Comparison of key physical parameters of various helicopters**

| | Physical characteristics | | | Computed characteristics | | | |
|---|---|---|---|---|---|---|---|
| Helicopter | Weight, N | Radius, m | Speed, rad/s | Scale ratio $N$ | Froude number | Mach number | $T_{\max}/W$ |
| UH-1H | 35,590 | 7.24 | 34 | 0.21 | 862 | 0.75 | 1.69 |
| R22 | 5,780 | 4.00 | 53 | 0.38 | 1,134 | 0.63 | 1.66 |
| R-50 | 431 | 1.52 | 89 | 1 | 1,230 | 0.41 | 1.75 |
| CMU R-50 | 667 | 1.52 | 89 | 1 | 1,230 | 0.41 | 1.12 |
| X-Cell | 44.5 | 0.76 | 167 | 2 | 2,165 | 0.38 | 3.64 |
| MIT X-Cell | 75.6 | 0.76 | 167 | 2 | 2,165 | 0.38 | 2.14 |

**Table 6 Rotor aerodynamic parameters for different helicopters near hover**

| Parameter | UH-1H | R22 | R-50 | CMU R-50 | X-Cell | MIT X-Cell |
|---|---|---|---|---|---|---|
| $N$ | 0.21 | 0.38 | 1 | 1 | 2 | 2 |
| $C_{T,\text{hover}}$ | 0.0028 | 0.0022 | 0.0027 | 0.0041 | 0.0013 | 0.0021 |
| DL, N/m$^2$ | 210 | 120 | 57 | 91 | 24 | 42 |
| $v_i$, m/s | 9.4 | 7.0 | 4.9 | 6.1 | 3.0 | 4.3 |
| $\lambda_i$ | 0.038 | 0.033 | 0.037 | 0.045 | 0.025 | 0.033 |
| $\text{Re}_{\text{tip}}$ | $8.8 \times 10^6$ | $3.1 \times 10^6$ | $9.6 \times 10^5$ | $9.6 \times 10^5$ | $5.1 \times 10^5$ | $5.1 \times 10^5$ |

Froude and Mach models. For the former, it follows that the hover thrust coefficient is unchanged by scale, whereas for the latter $c_T \propto 1/N$. Taking the X-Cell as a Mach scale model of the R-50 with $N = 2$, we indeed find that the X-Cell's thrust coefficient is around one-half that of the R-50 in both the instrumented ($c_{T,\text{R}-50} = 0.0041$ and $c_{T,\text{X}-\text{Cell}} = 0.0021$) and empty ($c_{T,\text{R}-50} = 0.0027$ and $c_{T,\text{X}-\text{Cell}} = 0.0013$) cases. Also note the similar thrust coefficient for the three Froude similar vehicles: the UH-1H, R22, and empty R-50 ($c_{T,\text{UH}-1\text{H}} = 0.0028$, $c_{T,\text{R22}} = 0.0022$, and $c_{T,\text{R}-50} = 0.0027$).

Because gross vehicle weight decreases faster than rotor disc surface area, another effect of scale is to decrease the rotor disc loading ($DL = T/A \propto 1/N$) and also the induced inflow velocity in hover:

$$v_{i,h} = \sqrt{DL/2\rho} \propto 1/\sqrt{N} \tag{24}$$

A smaller induced velocity means a smaller induced power $P_i = T v_i$, the principal power consumption in hovering flight. The induced power consumption decreases slightly faster than the hover thrust (vehicle weight): $T \propto 1/N^3$, and, thus, $P_i \propto 1/N^{7/2}$. Note, however, that other power expenditures, such as profile drag or gearbox friction, may be larger at smaller scale and offset this benefit. The inverse of the induced velocity is sometimes referred to as power loading[32] and is the ratio of thrust produced to rotor power consumed. As such, rotors with low disk loadings will require lower power per unit thrust. A consequence is that small-scale helicopters with smaller rotors will be able to carry proportionally heavier loads. Alternatively, a smaller but similar weight vehicle will require a proportionally smaller rotor.

Recall that the induced inflow ratio $\lambda_i$ (ratio of induced velocity to blade tip speed) for a rotor in hover is given by

$$\lambda_{i,h} = v_{i,h}/\Omega R = \sqrt{c_T/2} \tag{25}$$

Based on scaling relationships, this ratio should remain relatively unchanged for a Froude model, whereas for a Mach model, we obtain $\lambda_{i,h} \propto 1/\sqrt{N}$. These behaviors of inflow ratio can be observed in the numerical data of Table 6.

Table 6 lists other rotor aerodynamic quantities for the UH-1H, R22, R-50, and X-Cell as well. Overall, the variations among the parameters are consistent with the scaling hypotheses. Note that the Reynolds number, computed for flow over the blade tip, becomes smaller with decreasing vehicle size. This effect holds under both Froude and Mach scaling hypotheses, although the decrease occurs at different rates with increasing $N$. ($Re \propto 1/N^{3/2}$ for Froude and $Re \propto 1/N$ for Mach.) The range of Reynolds number given here is small enough that all vehicles operate in a turbulent flow regime. However, if a vehicle's size becomes too small, the blade aerodynamic conditions may change enough to challenge the basic assumption of a similar rotorcraft operating condition that underlies the scaling viewpoint. An example of an analysis of a microrotary-wing vehicle ($R = 7$ cm and $Re = 2.5 \times 10^5$), which raises small Reynolds number issues, is given in Ref. 33.

*Main Rotor Performance*

An important characteristic for helicopter maneuvering is the rotor thrust margin, which is the additional thrust available at a given operating condition. Traditional helicopters have small thrust margins in hover,[29] typically around 5–10%. It is possible to infer some rotor performance trends based on scaling alone. Note, however, that performance is ultimately a function of combined rotor and powerplant characteristics.

Mach scale models have proportionally faster rotor speeds than Froude scale models and, thus, hover at a lower thrust coefficient. The thrust coefficient reflects the lift loading of the rotor, that is, how much thrust is produced per disc area and rotor tip speed. To reflect the local lift loading of the rotor blades (with blade area $A_b$), consider the blade loading coefficient $c_T/\sigma$, given by

$$c_T/\sigma = [T/\rho A(\Omega R)^2](A/A_b) = T\Big/\rho A_b(\Omega R)^2 \tag{26}$$

The maximum blade loading coefficient is around 0.12 for a typical helicopter.[32] If the thrust is limited by the maximum blade loading coefficient, the maximum thrust of rotors as function of scale can be inferred from the expression

$$T_{\max} = (c_T/\sigma)_{\max}\rho A_b(\Omega R)^2 \tag{27}$$

This relation gives a maximum thrust that scales as $T_{\max} \propto 1/N^3$ for a Froude model and as $T_{\max} \propto 1/N^2$ for a Mach model. When divided by the vehicle weight $W \propto 1/N^3$, it follows that Froude models have a similar maximum thrust-to-weight ratio, consistent with the notion of dynamic similarity. However, for a Mach model, there is an increasing maximum thrust-to-weight: $(T/W)_{\max} \propto N$.

The flight-test identification experiments presented earlier include heave acceleration frequency responses to collective input (Fig. 10). From these responses, the maximum thrust-to-weight ratio in hover flight can be estimated. To compute the steady-state maximum acceleration, take the response values at 1 rad/s, which are $a_{z,\max} = 21$ m/s$^2$ and $a_{z,\max} = 11$ m/s$^2$ for the X-Cell and R-50, respectively. The maximum thrust-to-weight is obtained from

$$T_{\max}/W = ma_{z,\max}/mg = a_{z,\max}/g \tag{28}$$

which gives peak thrust-to-weight values of 2.1 and 1.1 for the X-Cell and R-50, respectively. Note that the ratio of these numbers agrees with the scaling predictions of a Mach-scaled model. The calculated maximum blade loading coefficient $(c_T/\sigma)_{\max}$ derived from these data is 0.1 and 0.09 for Carnegie Mellon University's (CMU's) R-50 and Massachusetts Institute of Technology's (MIT's) X-Cell, respectively.

To further illustrate the effect of scale on the maximum hover thrust-to-weight ratio $(T/W)_{\max}$, consider Fig. 11, which shows $(T/W)_{\max}$ for the sample vehicles, as well as the $(T/W)_{\max}$ curves corresponding to the Froude and Mach scaling effects. For the empty R-50, R22, and UH-1H, where no experimental data were available, $(T/W)_{\max}$ was computed with CMU's maximum blade loading coefficient, and the corresponding MIT X-Cell value was applied to the empty X-Cell. (Numerical thrust-to-weight data are listed in Table 5.) The R-50, R22, and UH-1H helicopters all lie along a line of similar $T/W$. Note that these values were computed for the empty weights; operational weights would reduce values closer to the CMU's R-50, in agreement with the 5–10% thrust margin. Both X-Cells relate well to the R-50s through the Mach scaling-parameterized $T/W$ curve. Note the extremely high value [$(T/W)_{\max} = 3.64$] obtained for the X-Cell, in agreement with the remarkable maneuverability of this vehicle. For completeness, a curve for yet another set of scaling rules based on constant rotor speed ($\Omega_m = \Omega_p$) is given.

**Table 7 Flying qualities parameters for R-50 and X-Cell based on identification results, with and without stabilizer bar, as well as expected ratios predicted by both Froude and Mach scaling considerations**

| | With stabilizer | | Without stabilizer | | Ratio | Scaling ratio | |
|---|---|---|---|---|---|---|---|
| Parameter | R-50 | X-Cell | R-50 | X-Cell | w/ stabilizer | Froude | Mach |
| Effective roll damping, $\frac{1}{s}$ | −48 | −98 | −7.6 | −17 | 2.0 | 1.4 | 2 |
| Control sensitivity, $\frac{\text{rad/s}^2}{\%}$ | 27.5 | 175 | 11.5 | 134 | 6.4 | 2 | 4 |
| Rate sensitivity, $\frac{\text{rad/s}}{\%}$ | 0.58 | 1.8 | 1.5 | 8.1 | 3.1 | 1.4 | 2 |
| Rate response time constant, s | 0.021 | 0.010 | 0.13 | 0.06 | 0.48 | 0.7 | 0.5 |

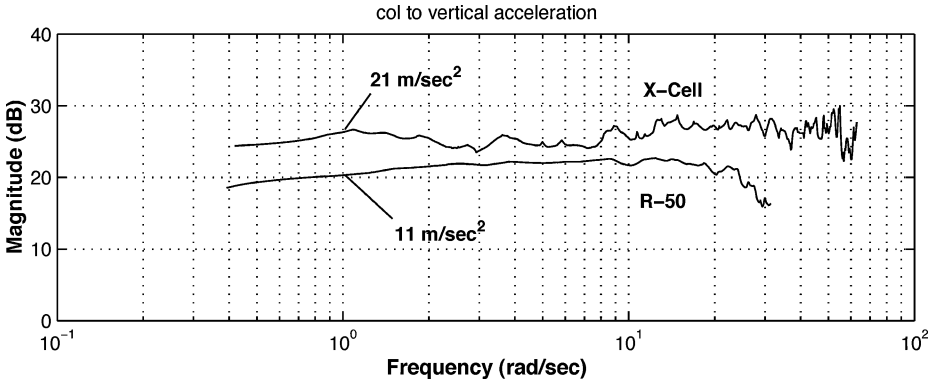


**Fig. 10 Identified collective cyclic to heave acceleration frequency responses in hover for R-50 and X-Cell helicopters.**

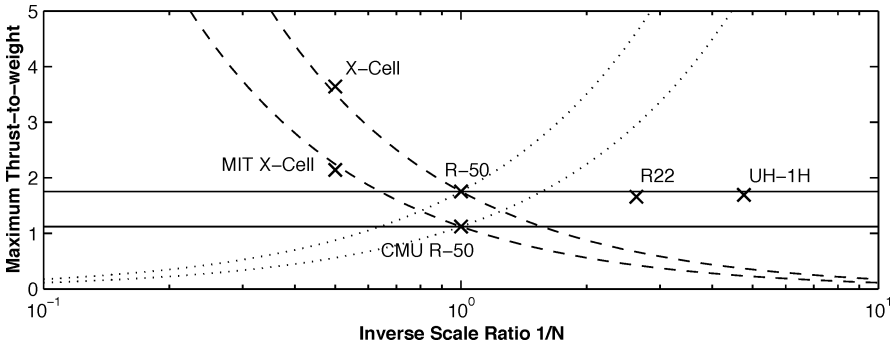


**Fig. 11 Estimated maximum thrust-to-weight ratio near hover for different full-scale and model-scale helicopters based on CMU's R-50 blade loading coefficient. Helicopters arranged in function of size relative to the R-50. The effect of scale on the thrust-to-weight ratio resulting from different rotor speed scaling rules is also shown: ———, Froude; - - - -, Mach; and · · · · ·, constant rotor speed.**

The mentioned earlier, lower hover inflow ratio trends have a direct implication on the amount of heave damping and the maximum vertical velocity $w_{\max}$, whose value is a function of the rotor tip speed[29]:

$$w_{\max} = -\tfrac{4}{3}\Omega R\Theta_0 \tag{29}$$

Hence, Froude models should exhibit a slight decrease in maximum vertical velocity, that is, $w_{\max} \propto 1/\sqrt{N}$, whereas Mach models should exhibit a similar maximum climb velocity, consistent with the initial notion of Mach scaling.

*Angular Flying Qualities*

To complete the analysis of scale-dependent performance capabilities, we now look at the effect of vehicle size on the angular FQ parameters presented earlier. The effects can be inferred directly from the relationships between time constant and scale factor [Eqs. (19) and (22) for the Froude and Mach models, respectively]. This deduction is possible because the FQs listed in Table 3 have units derived only from timescale, angle, and input magnitude, the latter two of which are independent of rotorcraft size.

The expressions in Table 3 show that when a Froude-scaled smaller helicopter (increasing $N$) is considered, control sensitivity increases proportionally to scale factor, rate sensitivity increases as the square root of the scale factor, and rate response time constant decreases inversely as the square root of scale (an increase in bandwidth by a factor $\sqrt{N}$). Each of these effects make a small-scale helicopter more agile and responsive, but also more difficult to control manually; this explains the necessity of the stabilizer bar for effective piloted operation. Note the even more dramatic effects associated with Mach scaling.

For computer controlled operations, the stabilizer bar is not required, and the added agility resulting from scaling may represent an operational advantage. If desired, the effect of the stabilizer bar can be obtained by the use of a simple feedback loop like that already implemented for yaw damping.

Given the identified state-space model parameters of Table 1, FQ values for the R-50 and X-Cell are readily computed (Table 7).

Quantities are calculated for the vehicles with and without the stabilizer bar. The latter set of numbers are, of course, extrapolations because the identification data were never collected without stability augmentation. By comparison of the computed FQ ratios to those predicted by scaling, it again seems that the R-50 and X-Cell are better related by Mach scaling than by dynamic similarity. Note also the stabilizer bar's significant "taming" effect on effective roll damping and rate sensitivities.

*Maneuvering and Flight Operations*

Simple level-flight maneuvers illustrate the combined effect of scaling and design on flight operations. Consider first the steady mid-to-long-duration coordinated turn and rectilinear acceleration, which give indications of scale-dependent geometrical characteristics. Also, short-duration side-step-type maneuvers are important in rotorcraft operation and emphasize angular agility.

At a given speed, the minimum turn radius is determined by the maximum thrust-to-weight ratio $\bar{L}$. We can employ the maximum vertical acceleration $a_{z,\max}$ used in Eq. (27) to calculate an approximate value, that is, $\bar{L} \approx a_{z,\max}/g = 1.1$ for CMU's R-50 and $\bar{L} \approx 2.1$ for MIT's X-Cell. Note that the identified hover values represent conservative estimates because in forward flight, more thrust can be generated due to the decrease in rotor-induced inflow velocity.[29] These values result in maximum bank angles $\bar{\phi}$ of about 25 deg for CMU's R-50 and 62 deg for MIT's X-Cell. The minimum turn radius is then approximated by

$$\rho_{\min} \approx v^2/\bar{L}\sin\bar{\phi} \tag{30}$$

Evaluation of this expression for $v = 5$ m/s (altitude 15 m/s) gives $\rho_{\min} = 1.4$ m (altitude 12 m) for MIT's X-Cell, and 5.6 m (altitude 50 m) for CMU's R-50. The R-50 would, therefore, take about four times more space than the X-Cell to execute a 180-deg turn, which at faster speeds can mean a serious operational handicap.

The maximum rectilinear acceleration can also be estimated from these values. Specifically, $\bar{a}_x \approx \bar{L}\sin\bar{\phi} = 1.89g$ and $0.5g$ for the instrumented X-Cell and R-50, respectively. In terms of rectilinear motion, the X-Cell exceeds the gravitational acceleration in all three dimensions, which makes it possible to virtually cancel the effect of gravity. From earlier scaling considerations for the maximum thrust, together with pitching/rolling kinematics, it follows that for a Mach model, $\bar{a}_x$ and $\bar{a}_y \propto N$. Simple constant-acceleration kinematics show that the time to achieve some absolute velocity change scales as $1/N$, and the time to achieve a given displacement (at constant acceleration) is proportional to $1/\sqrt{N}$. For a Froude scale model, there is no variation with scale.

Small displacement corrections in the form of side steps can be used in hover flight to reposition a rotorcraft, or in cruise flight to correct a cross-track error. For these short-term maneuvers, angular agility is the dominant effect. The earlier stated observation that angular acceleration per unit cyclic control input varies as $N^2$ for Mach models and as $N$ for Froude models means that the time required to achieve some angular change in the thrust vector varies as $1/N$ for Mach models and as $1/\sqrt{N}$ for Froude models. Given the foregoing rectilinear relations, it follows that combined angular–translational maneuvers should be $1/N$ faster for Mach models and no more than $1/\sqrt{N}$ faster for Froude models.

When large rectilinear acceleration is combined with high angular sensitivity in small-scale rotorcraft like the X-Cell, fast yet compact maneuvers can be executed, and quick redirections of the thrust vector and, thus, rapid changes in the flight direction, can be obtained. Moreover, with specially designed rotors, inverted flight can be achieved fairly easily. These characteristics result in capabilities unseen in typical manned helicopters.

## Conclusions

This paper described the dynamics of miniature rotorcraft from the perspectives of physical modeling and identification, flying qualities, and scaling. An identified linear model captures the key dynamic characteristics of helicopters with a relatively small set of parameters, many of which can be numerically verified with laboratory measurements, validating the model's physical significance. The model structure is general enough to describe both hover and cruise flight conditions for two differently sized miniature rotorcraft and allows easy evaluation of several important flying qualities metrics.

These flying qualities provide simple measures of vehicle performance, describing the fundamental dynamic capabilities of a given rotorcraft. For example, input response timescales and control sensitivities based on angular dynamics give basic metrics of vehicle agility and provide a link between physical design variables and performance characteristics. Also, the flying qualities make clear the beneficial effects of stabilizer bar mechanisms on open-loop pilot controllability.

In addition, physical scale has been introduced as a parameter for describing rotorcraft dynamics across a wide range of vehicle sizes. A series of simple relationships based on two fundamental scaling hypotheses helped quantify the intuitive notion that small-sized rotorcraft tend to be more agile and responsive than their larger-scaled counterparts. The scale-based viewpoint predicts trends in flying qualities, rotor performance, and vehicle maneuverability, providing specific references for vehicle design and control system requirements. From this perspective, we see that when conceiving a small-scale rotorcraft based on some larger prototype, the engineering design space expands rapidly with decreasing length scale. The faster response characteristics brought on by reduced size allow the engineer to choose a vehicle design ranging from agile Mach-scaled behavior on one hand to slower Froude characteristics on the other, as well as any desired behavior in between. Finally, miniature rotorcraft, with their overall faster dynamics, will set more stringent bandwidth requirements on various hardware and computing components.

## Acknowledgments

Partial funding for this research was provided by the NASA Grant NAG 2-1441 and by the U.S. Office of Naval Research under a Young Investigator Award. The authors thank Omead Amidi, Mark DeLouis, Ryan Miller, and Takeo Kanade for conceiving and making possible the autonomous helicopter project at Carnegie Mellon University. Mark Tischler (NASA Ames Research Center) and Howard Curtiss (Princeton University) made important contributions to the basic formulation of this work. The authors are also grateful to Vlad Gavrilets, Ioannis Martinos, Kara Sprague, and Raja Bortcosh for the development and flight testing of Massachusetts Institute of Technology's miniature helicopter.

## References

[1]Amidi, O., Kanade, T., and Miller, R., "Vision-Based Autonomous Helicopter Research at Carnegie Mellon Robotics Institute," Heli Japan '98, Paper T7-3, Gifu, Japan, 1998.

[2]Blaurock, C., Brown, P., Dyer, K., Elliot, P., Eremenko, P., Farah, J., Feron, E., Frazzoli, E., Gavrilets, V., Hallam, C., Lundgren, A., MacIvor, D., Narendran, K., Perdichizzi, D., Rasmussen, S., and Chisholm, T., "The MIT Entry into the 1998 AUVS International Aerial Robotics Competition," Association for Unmanned Vehicle Systems International (AUVSI), June 1998.

[3]Sanders, C. P., DeBitetto, P. A., Feron, E., Vuong, H. F., and Leveson, N., "Hierarchical Control of Small Autonomous Helicopters," *Proceedings of the 37th IEEE Conference on Decision and Control*, IEEE Publications, Piscataway, NJ, 1998, pp. 3629–3634.

[4]Heffley, R. K., and Mnich, M. A., "Minimum-Complexity Helicopter Simulation Math Model," NASA, U.S. Army Aviation Systems Command USAAVSCOM TR 87-A-7, Moffett Field, CA, April 1987.

[5]McRuer, D. T., Ashkenas, I., and Graham, D., *Aircraft Dynamics and Automatic Control*, Princeton Univ. Press, Princeton, NJ, 1973, Chap. 4.

[6]Hansen, R. S., "Toward a Better Understanding of Helicopter Stability Derivatives," *Journal of the American Helicopter Society*, Vol. 29, No. 1, 1982, pp. 15–24.

[7]Tischler, M. B., "System Identification Requirements for High-Bandwidth Rotorcraft Flight Control System Design," *Journal of Guidance, Control, and Dynamics*, Vol. 13, No. 5, 1990, pp. 835–841.

[8]Ham, J. A., Gardner, G. K., and Tischler, M. B., "Flight-Testing and Frequency-Domain Analysis for Rotorcraft Handling Qualities," *Journal of the American Helicopter Society*, Vol. 40, No. 2, 1995, pp. 28–38.

[9]Bruce, P. B., Silva, J. E. F., and Kellett, M. G., "Maximum Likelihood Identification of a Rotary-Wing RPV Simulation Model From Flight-Test Data," *Proceedings of the AIAA Atmospheric Flight Mechanics Conference and Exhibit*, AIAA, Reston, VA, 1998, pp. 126–134; also AIAA Paper 98-4157.

[10]Kim, A. K., and Tilbury, D. M., "Mathematical Modeling and Experimental Identification of a Model Helicopter," *Proceedings of the AIAA Modeling and Simulations Technology Conference*, AIAA, Reston, VA, 1998, pp. 203–213; also AIAA Paper 98-4357.

[11]Morris, J., Nieuwstadt, M. V., and Bendotti, P., "Identification and Control of a Model Helicopter in Hover," *Proceedings of the American Control Conference*, American Automatic Control Council, 1994, pp. 1238–1242.

[12]Tischler, M. B., and Cauffman, M. G., "Comprehensive Identification from Frequency Responses; an Interactive Facility for System Identification and Verification, Class Notes and User's Manual," NASA Ames Research Center, USAATCOM TR-94-A-017, TR-94-A-018, Moffett Field, CA, Sept. 1994.

[13]Mettler, B., Tischler, M. B., and Kanade, T., "System Identification Modeling of a Small-Scale Unmanned Rotorcraft for Control Design," *Journal of the American Helicopter Society*, Vol. 47, No. 1, 2002, pp. 50–63.

[14]Gavrilets, V., Mettler, B., and Feron, E., "Nonlinear Model for a Small-Size Acrobatic Helicopter," *Proceedings of the AIAA Guidance, Navigation, and Control Conference*, Vol. 3, AIAA, Reston, VA, 2001, pp. 1593–1600.

[15]Tischler, M. B., and Cauffman, M. G., "Frequency-Response Method for Rotorcraft System Identification: Flight Application to BO-105 Coupled Rotor/Fuselage Dynamics," *Journal of the American Helicopter Society*, Vol. 37, No. 3, 1992, pp. 3–17.

[16]Fletcher, J. W., "Identification of UH-60 Stability Derivative Models in Hover from Flight Test Data," *Journal of the American Helicopter Society*, Vol. 40, No. 1, 1995, pp. 32–46.

[17]Williams, J. N., Ham, J. A., and Tischler, M. B., "Flight Test Manual," U.S. Army Aviation Technical Test Center, AQTD Project 93-14, Edwards AFB, CA, 1995.

[18]Miller, R. H., "A Method for Improving the Inherent Stability and Control Characteristics of Helicopters," *Journal of the Aeronautical Sciences*, Vol. 17, No. 6, 1950, pp. 363–374.

[19]Mettler, B., Tischler, M. B., and Kanade, T., "System Identification of Small-Size Unmanned Helicopter Dynamics," *Proceedings of the 55th Forum of the American Helicopter Society*, American Helicopter Society, Alexandria, VA, 1999, pp. 1706–1717.

[20]Mettler, B., *Identification Modeling and Characteristics of Miniature Rotorcraft*, Kluwer Academic, Boston, MA, 2002, Chap. 4.

[21]Mettler, B., Tischler, M. B., Kanade, T., and Messner, W., "Attitude Control Optimization for a Small-Scale Unmanned Helicopter," *Proceedings of the AIAA Guidance, Navigation, and Control Conference and Exhibit*, AIAA, Reston, VA, 2000, pp. 459–468.

[22]Mettler, B., Gavrilets, V., Feron, E., and Kanade, T., "Flight-Test Evaluation of Dynamic Compensation for High-Bandwidth Control of Small-Scale Helicopter," American Helicopter Society Test and Evaluation TE3(3), Jan. 2002.

[23]LaCivita, M., Messner, W. C., and Kanade, T., "Modeling of Small-Scale Helicopters with Integrated First-Principles and System Identification Techniques," *Proceedings of the 58th Forum of the American Helicopter Society*, American Helicopter Society, Alexandria, VA, 2002, pp. 2505–2516.

[24]Gavrilets, V., Martinos, I., Mettler, B., and Feron, E., "Control Logic for Automated Aerobatic Flight of Miniature Helicopter," *Proceedings of the AIAA Guidance, Navigation, and Control Conference*, Vol. 2, AIAA, Reston, VA, 2002, pp. 1470–1478.

[25]Gavrilets, V., Martinos, I., Mettler, B., and Feron, E., "Aggressive Maneuvering Flight Tests of a Miniature Robotic Helicopter," *Experimental Robotics VIII*, Springer, Berlin, 2003.

[26]Heffley, R. K., "A Compilation and Analysis of Helicopter Handling Qualities Data; Volume II: Data Analysis," NASA CR-3145, March 1979.

[27]Timoshenko, S., Young, D. H., and Weaver, W., Jr., *Vibration Problems in Engineering*, Wiley, New York, 1974, Chap. 1.

[28]Johnson, W., *Helicopter Theory*, Princeton Univ. Press, Princeton, NJ, 1980, Chaps. 10, 15.

[29]Padfield, G. D., *Helicopter Flight Dynamics: The Theory and Application of Flying Qualities and Simulation Modeling*, AIAA Education Series, AIAA, Reston, VA, 1996, pp. 38–40.

[30]Curtiss, H. C., Putman, W. F., and Martinez, E., "The Evaluation of Stability and Control Characteristics of Aircraft at Low Speed Using Dynamically Similar Models in Semi-Free Flight," *18th Annual Forum of the American Helicopter Society*, American Helicopter Society, Alexandria, VA, 1962, pp. 122–131.

[31]Friedmann, P. P., "Aeroelastic Scaling For Rotary-Wing Aircraft with Applications," *Proceedings of the 42nd AIAA/ASME/ASCE/AHS/ASC Structures, Structural Dynamics, and Materials Conference*, AIAA, Reston, VA, 2001, pp. 1–15; also AIAA Paper 2001-1534.

[32]Leishman, J. G., *Principles of Helicopter Aerodynamics*, Cambridge Univ. Press, Cambridge, England, U.K., 2000, pp. 42–43.

[33]Bohorquez, F., Samuel, P., Sirohi, J., Pines, D., Rudd, L., and Perel, R., "Design, Analysis and Hover Performance of a Rotary Wing Micro Air Vehicle," *Journal of the American Helicopter Society*, Vol. 48, No. 2, 2003, pp. 80–90.